Recognition of Multivalent Histone States Associated with Heterochromatin by UHRF1 Protein*□S

Nataliya Nady[‡], **Alexander Lemak**[‡1], **John R. Walker**[§1], **George V. Avvakumov**[§1], **Michael S. Kareta**[¶1],
Mayada Achour[||], **Sheng Xue**[§], **Shili Duan**[‡], **Abdellah Allali-Hassani**[§], **Xiaobing Zuo**[**], **Yun-Xing Wang**[**],
Christian Bronner[||], **Frédéric Chédin**[¶], **Cheryl H. Arrowsmith**[‡§2], and **Sirano Dhe-Paganon**[§‡‡3]

From the [‡]*Ontario Cancer Institute, Campbell Family Cancer Research Institute and Department of Medical Biophysics, University of Toronto, Toronto, Ontario M5G 1L7, Canada, the* [§]*Structural Genomics Consortium, University of Toronto, Toronto, Ontario M5G 1L7, Canada, the* [¶]*Department of Molecular & Cellular Biology, University of California, Davis, California 95616,* [||]*CNRS UMR7213, Laboratoire de Biophotonique et Pharmacologie, Faculté de Pharmacie, 74 route du rhin, 67401 Illkirch cedex, France, the* [**]*Protein Nucleic Acid Interaction Section, Structural Biophysics Laboratory, NCI-Frederick, National Institutes of Health, Frederick, Maryland 21702, and the* [‡‡]*Department of Physiology, University of Toronto, Toronto, Ontario M5G 1L5, Canada*

Histone modifications and DNA methylation represent two layers of heritable epigenetic information that regulate eukaryotic chromatin structure and gene activity. UHRF1 is a unique factor that bridges these two layers; it is required for maintenance DNA methylation at hemimethylated CpG sites, which are specifically recognized through its SRA domain and also interacts with histone H3 trimethylated on lysine 9 (H3K9me3) in an unspecified manner. Here we show that UHRF1 contains a tandem Tudor domain (TTD) that recognizes H3 tail peptides with the heterochromatin-associated modification state of trimethylated lysine 9 and unmodified lysine 4 (H3K4me0/K9me3). Solution NMR and crystallographic data reveal the TTD simultaneously recognizes H3K9me3 through a conserved aromatic cage in the first Tudor subdomain and unmodified H3K4 within a groove between the tandem subdomains. The subdomains undergo a conformational adjustment upon peptide binding, distinct from previously reported mechanisms for dual histone mark recognition. Mutant UHRF1 protein deficient for H3K4me0/K9me3 binding shows altered localization to heterochromatic chromocenters and fails to reduce expression of a target gene, *p16^{INK4A}*, when overexpressed. Our results demonstrate a novel recognition mechanism for the combinatorial readout of histone modification states associated with gene silencing and add to the growing evidence for coordination of, and cross-talk between, the modification states of H3K4 and H3K9 in regulation of gene expression.

Histone modifications and DNA methylation represent two layers of heritable epigenetic information that regulate chromatin structure and gene activity in eukaryotic organisms. Methylated DNA sequences are generally associated with long term transcriptional silencing through the recruitment of repressor complexes, including methyl-binding proteins, histone deacetylases, and chromatin remodeling machinery (1, 2). Likewise, specific histone methylation states can recruit multivalent adaptor proteins, which lead to chromatin condensation, further inhibiting gene expression. Accumulating evidence shows that these two methylation systems act cooperatively to establish the epigenetic state of the cell (3–5); however, the mechanisms of this cooperation remain vague.

During replication, CpG methylation patterns are maintained in mammals by the DNA methyltransferase 1 with hemimethylated CpG dinucleotides serving as a substrate. This enzyme is aided by UHRF1 (<u>u</u>biquitin-like, <u>P</u>HD and <u>R</u>ING <u>fi</u>nger containing <u>1</u>, also known as ICBP90 in humans and NP95 in mouse), which interacts with DNA methyltransferase 1 and specifically recognizes hemimethylated CpG dinucleotides through its SET- and RING-associated domain (SRA)[4] (6, 7).

UHRF1 also has been implicated in histone methylation-associated activities related to pericentric heterochromatin (6–12). For example, UHRF1 is found in a complex with both methylated histones (8, 13) and histone-modifying enzymes such as HDAC1 and KMT1C/G9a (14, 15). UHRF1 also interacts with H3K9me3-containing nucleosomes, and this interaction is potentiated by DNA methylation (3). Thus, it is not surprising that UHRF1 deficiency leads not only to decreased levels of DNA methylation (6, 7) but also to impaired maintenance of heterochromatin structure (8, 10, 16) and increased transcription of major satellites, regions that make up the bulk of pericentric heterochromatin.

UHRF1 has significant affinity for H3K9me3 (8, 13), but the mechanism of this interaction remains unclear. In addition to the SRA domain, UHRF1 contains other conserved domains (see Fig. 1a), including a ubiquitin-like domain (ubl), a plant homeobox domain (PHD) that has been implicated in the UHRF1 binding to both DNA methyltransferase 1 (6) and H3K9me3 (8), and a RING E3 ligase domain (RING). Here, we provide biochemical and cell-based evidence for the mechanism of the UHRF1 binding to histone H3 in which Lys-9 is trimethylated and Lys-4 is unmodified or monomethylated. Furthermore, our structural analysis revealed a novel mode of interaction enabling combinatorial readout of a multivalent state within a single H3 tail.

EXPERIMENTAL PROCEDURES

Cloning, Protein Expression, and Purification—The cDNA-encoding residues 121–286 of the human UHRF1 protein was cloned into a modified pET28a bacterial expression vector encoding an N-terminal hexahistidine fusion protein with a tobacco etch virus protease cleavage site. Mutated cDNAs were made by using QuikChange II XL Site-directed mutagenesis kit (Stratagene); mutations were confirmed by sequencing complete cDNAs. The protein was expressed in *Escherichia coli* BL21(DE3) grown in Terrific Broth in the presence of 50 μg/ml of kanamycin and induced with 0.2 mM isopropyl-1-thio-D-galactopyranoside. The protein was purified using affinity, gel filtration, and ion exchange chromatography, with details provided in the supplemental material. Note that the protein was not stable at low salt concentrations; thus, for binding assays and structure determination, buffers contained at least 250 mM NaCl. Details of sample preparations for crystallographic, solution NMR, and small angle x-ray scattering studies are provided in the Supplementary Information section.

Peptides used for NMR, crystallization and small angle x-ray scattering were purchased in purified form from Tufts University Core Services (Boston, MA). Two peptides were used for these studies, the peptide TARK(me3)ST corresponding to the N-terminal histone H3 residues 6–11, hereby referred to as "short peptide" or H3K9me3, and the peptide ARTKQTARKme3ST corresponding to the histone H3 residues 1–11, also referred to as the long or H3K4me0/K9me3 peptide.

Crystallization, Data Collection, Structure Solution, and Refinement—Crystals of the selenomethionine derivative of UHRF1 tandem Tudor domain (TTD) were grown at 18 °C using the hanging drop method by mixing 1:1 (v/v) of 23 mg/ml

protein solution with a well solution consisting of 10% PEG 8000, 0.2 M $(NH_4)_2SO_4$, 0.1 M sodium cacodylate, pH 6.5, and 1 mM tris(2-carboxyethyl) phosphine. The crystals were cryoprotected by immersion in the well solution mixed in a 1:1 ratio with a water solution of 20% (w/v) sucrose, 4% (w/v) glucose, 18% (v/v) glycerol, and 18% (v/v) ethylene glycol, frozen, and stored in liquid nitrogen. Data from crystals of the selenomethionine derivative of the UHRF1 TTD were collected at NSLS beamline X29 at the selenium peak wavelength (0.97942 Å) and processed using the HKL2000 program suite (17). Solve and Resolve were used to locate the selenium substructure and to build the initial model (18, 19). A second data set collected on beamline GM/CA-CAT 23ID-B at the Advanced Photon Source at 1.0000 Å, which extended to higher resolution and with greater completeness, was used for the final refinement of the structure. Data from crystals of selenomethione labeled UHRF1 TTD that had been soaked with a six-residue peptide from H3 (TARKme3ST) were collected at SBC-CAT 19ID at the Advanced Photon Source at 0.99987 Å and processed using HKL2000. Data from all crystals was collected at 100 K. Manual model building was carried out using the graphics program Coot (20). Refinement was carried out for both the apo and complex structures using the CCP4 program REFMAC (21). In the later stages of refinement, translation libration screw motion (TLS) and restrained refinement was carried out, with the initial TLS parameters obtained from the TLS motion determination (TLSMD) web server (22). The MolProbity Ramachandran plot showed that 97.58 and 93.23% of the residues were in the most favored region for apo and liganded structures, respectively, whereas the rest were in the allowed region.

Histone Peptide SPOT Blot Peptide Array Screen and Fluorescence Polarization Binding Assays—Peptides were synthesized directly on a modified cellulose membrane with a polyethylglycol linker using the peptide synthesizer MultiPep (Intavis). The binding reaction was initially performed using a library of 580 membrane-immobilized peptides corresponding to control peptides and 8–14-residue-long stretches of histones H2A, H2B, H3, and H4 sequences with either nonmodified or variously modified arginine, lysine, serine, and threonine residues (one modified residue per peptide) as described previously (23). The subsequent peptide libraries were designed specifically to test the binding preference of UHRF1 TTD domain to H3K4 and K9 marks.

For fluorescence polarization (FP) studies, peptides indicated in the figures were synthesized, N-terminally labeled with fluorescein, and purified by Tufts University Core Services (Boston, MA). Binding assays were performed in a 10-μl volume at a constant labeled peptide concentration of 36 nM, and the protein was used at concentrations at saturation ranging between 800 and 1300 μM in buffer containing 20 mM Tris, pH 8.0, 250 mM NaCl, 1 mM DTT, 1 mM benzamidine, 1 mM PMSF, 0.01% Tween 20. FP assays were performed in 384-well plates using Synergy 2 microplate reader (BioTek). The excitation wavelength of 485 nm and the emission wavelength of 528 nm were used. The data were corrected for background of the free labeled peptides. To determine K_d values, the data were fit to a hyperbolic function using Sigma Plot software (Systat Software,

Inc.). The K_d values represent averages ± S.E. for at least three independent experiments.

NMR Spectroscopy and Data Analysis—Chemical shift mapping on the UHRF1 TTD domain was done by monitoring the ^{1}H-^{15}N HSQC spectra of the uniformly ^{15}N-labeled TTD domain alone (0.45 mM) and with an excess of unlabeled interacting short or long H3 peptides. Aliquots of unlabeled peptides were titrated into the labeled TTD domain in molar ratio 1:35 for the short peptide and 1:5 for the long peptide until no further changes in chemical shifts were detected in the ^{1}H-^{15}N HSQC spectrum. The HSQC spectra were recorded at 25 °C in 20 mM NaPi, pH 7.0, 250 mM NaCl, 2 mM DTT, 1 mM benzamidine, 0.5 mM PMSF and supplemented with 10% (v/v) D_2O on a Bruker Avance 800-MHz spectrometer. Composite chemical shift perturbation values shown were calculated using the equation $\Delta_{comp} = (\Delta\delta^2_{HN} + (\Delta\delta_N/6.5)^2)^{1/2}$. The dissociation constant K_d was estimated by fitting the observed chemical shift changes for selected residues to the following equation, $\Delta = \Delta_{max}([L]_T + [P]_T + K_d - (([L]_T + [P]_T + K_d)^2 - 4[L]_T[P]_T)^{1/2})/(2[P]_T)$, in which Δ is the observed chemical shift change at a given total ligand concentration ($[L]_T$), Δ_{max} is the change in chemical shift at saturation, and $[P]_T$ is the total protein concentration. Data were fitted using GraphPad Prism software.

For structure determination, NMR spectra were recorded at 25 °C on a Varian INOVA 600-MHz spectrometer equipped with triple resonance probe and Bruker Avance 600- and 800-MHz spectrometers equipped with cryoprobes. NMR data were collected at high resolution from nonlinearly sampled spectra and processed using multidimensional decomposition (24, 25) and NMRPipe software (26). The data were analyzed with NMRView and Sparky software (27). The details of structure calculation are indicated in the supplemental material.

Residual Dipolar Coupling (RDC) Measurements and Analysis—Dipolar couplings were measured on isotropic and anisotropic sample containing 0.6 mM ^{15}N,^{13}C-labeled TTD protein and 3 mM unlabeled H3K4me0/K9me3 peptide. ^{15}N-^{1}HN residual dipolar couplings were extracted from two-dimensional in-phase/anti-phase (IPAP) ^{15}N-^{1}HN HSQC spectra (28). Pulse sequences that were used for measurement of ^{13}C′-^{13}Ca couplings have been described earlier (29). Pulse sequences for ^{15}N-^{13}C′ are courtesy of Lewis Kay. The aligned sample from which ^{15}N-^{1}HN, ^{15}N-^{13}C′, and ^{13}C′-^{13}Ca RDCs were extracted contained 3.3% final sample volume of C12E5 PEG/hexanol medium (deuterium splitting, 13.2 Hz; line width, 1.5 Hz) (30), and 219 couplings were used. The aligned sample, from which ^{15}N-^{1}HN RDCs were extracted, contained total volume 6% C12E5 PEG/hexanol medium (deuterium splitting, 25 Hz; line width, 1.8 Hz) (30), 102 couplings were used, and another sample was prepared by adding 10 mg/ml *Pf1* bacteriophage (deuterium splitting, 12 Hz; line width, 1.7 Hz) (31), and 95 couplings were used. FuDA software was used to extract peak shape and intensity parameters from J-evolution ^{15}N-^{13}C′, and ^{13}C′-^{13}Ca RDCs.

Another set of ^{15}N-^{1}HN residual dipolar couplings was measured on isotropic and anisotropic sample containing only 0.6 mM ^{15}N,^{13}C-labeled TTD protein. The aligned sample contained 3.2% final sample volume of C12E5 PEG/hexanol medium (deuterium splitting, 16 Hz; linewidth, 1.8 Hz) (30); 73 couplings were used.

To obtain goodness of fit (Q) values for experimental RDC values with theoretically back-calculated values for the apo crystal structure and complex (TTD/H3K4me0K9me3) NMR structures, the data were analyzed using PALES (33). The plots were produced with MODULE (version 1.0) (34).

Cell Culture and Immunocytochemistry—$Np95^{-/-}$ ES cells and their wild-type counterpart (E14) were a kind gift from Drs. Haruhiko Koseki and Masahiro Muto. Cells were grown as described (6) and passaged every other day. The overall growth characteristics of the stably expressing cells were not significantly different from the parent $Np95^{-/-}$ cells or from the wild-type E14 cells. Expression vectors carried the *mUhrf1* cDNA under a cytomegalovirus early enhancer element and chicken β-actin promoter (CAG) promoter. The *mUhrf1* cDNA was preceded immediately by an in-frame hemagglutinin (HA)-encoding sequence, thus leading to the expression of an N-terminal HA-tagged UHRF1 protein. An internal ribosome entry site (IRES)-puromycin cassette was inserted immediately downstream of the *Uhrf1* coding sequence and allowed selection of UHRF1-expressing clones through puromycin selection. Cells were transfected using TurboFect (Fermentas) and selected with 1 μg/ml of puromycin starting 36–48 h post-transfection. Clones were picked after 14 days under selection and expanded. Expression levels were determined by Western blots. Transfection of the cells with mUHRF1^{F148A} mutant was similarly performed. The relative expression levels of the wild-type and mutated mUHRF1 proteins were similar to each other and comparable with the expression levels of the endogenous UHRF1 protein in E14 cells as assayed by quantitative Western blots using a direct anti-UHRF1 monoclonal antibody (1RC1C-10).

Close examination of the $Np95^{-/-}$ cell line revealed that an unexpected splicing event from exons 1 to 8, which immediately flank the region that was targeted for gene replacement, drives the production of a truncated UHRF1 protein lacking coding exons 2 to 7 (supplemental Fig. S9). This truncated UHRF1 remnant, referred to as UHRF1Δ(2–7), lacks the ubiquitin-like domain, TTD, and PHD domains, but still carries intact SRA and RING domains. Due to the presence of the SRA domain, it is likely that UHRF1Δ(2–7) can bind to hemimethylated DNA. Thus, the $Np95^{-/-}$ cell line is not well suited for analyzing the role of UHRF1 in maintenance DNA methylation. The reintroduced UHRF1 proteins carried an N-terminal HA epitope tag allowing for discrimination between the transgene and endogenous UHRF1Δ(2–7).

For immunocytochemistry, cells were seeded onto glass coverslips coated with 0.1% gelatin. After 24 h of growth, the cells were harvested, washed with PBS, and fixed with 2% formaldehyde in PBS for 10 min. The cells were washed twice with PBS and permeabilized with 1% Triton X-100 in PBS for 10 min. Cells were then incubated in blocking buffer (3% BSA, 0.1% Tween 20, 4× SSC) for 20 min and immunostained with a rabbit anti-H3K9me3 antibody (Millipore catalog no. 07-523) at a 1:1000 dilution and with a mouse anti-HA antibody (Covance, MMS-101P) at a 1:750 dilution, and both were diluted in blocking buffer. The cells were further washed in blocking buffer and
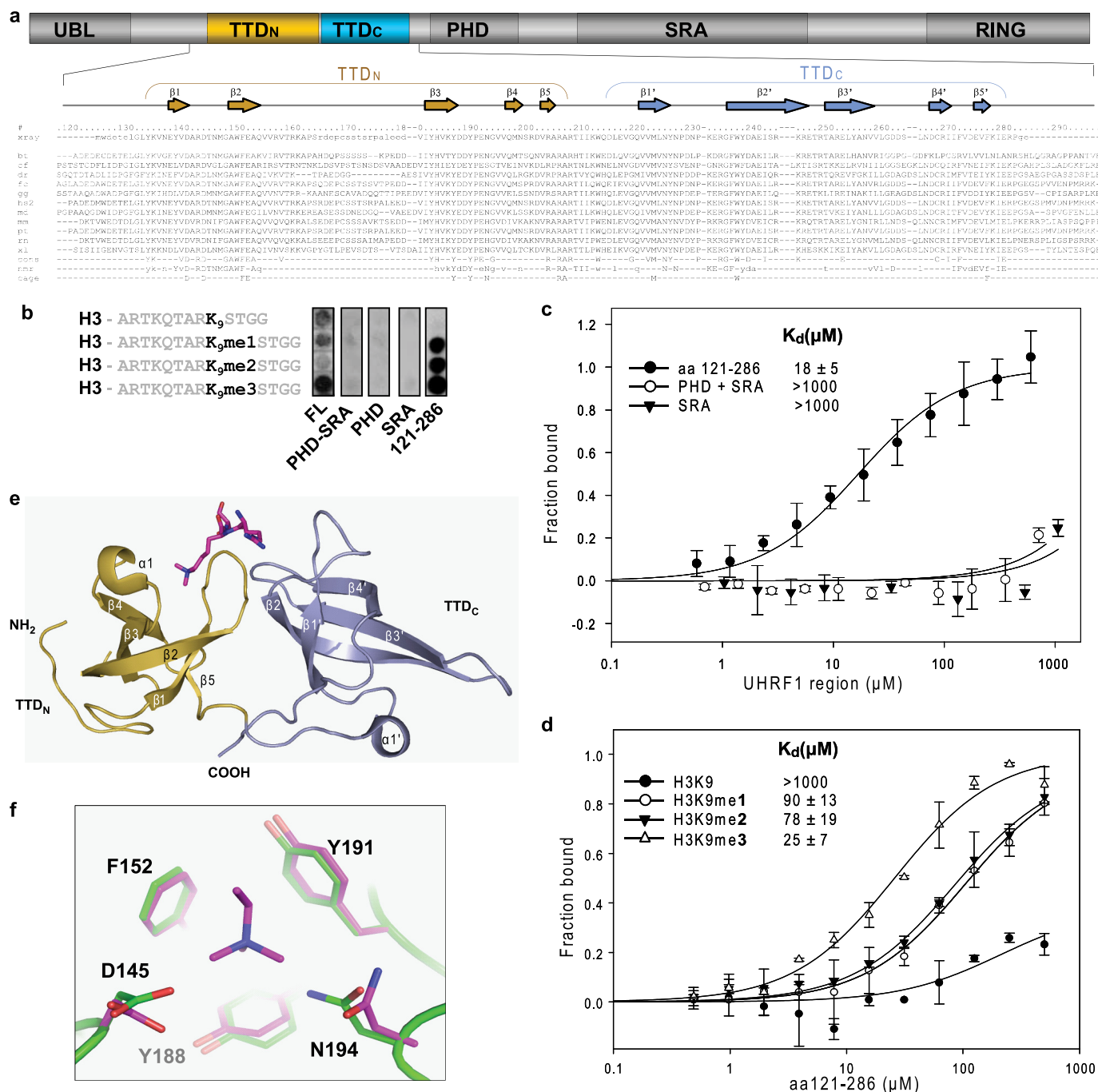
FIGURE 1. **A novel tandem tudor domain (TTD) within UHRF1 preferentially binds H3 histone tail trimethylated at Lys-9.** *a*, domain composition of UHRF1 includes ubiquitin-like (UBL), TTD, comprising N- and C-terminal subdomains (TTD$_N$, TTD$_C$), PHD, SRA, and RING domains. The human UHRF1 protein sequence (amino acids 119–298) is aligned with that of other species (*bt, Bos taurus; cf, Canis familiaris; dr, Danio rerio; fc, Felis catus; gg, Gallus gallus; hs2, Homo sapiens; md, Monodelphis domestica; mm, Mus musculus; pt, Pan troglodytes; rn, Rattus norvegicus; xl, Xenopus laevis*); the *lowercase sequences* are flexible regions in the liganded x-ray structure. The residue numbering corresponds to the human UHRF1 sequence. Drawn *above the number line* are secondary structure elements and their labels. Residues that are fully conserved (cons) undergo medium and strong (*uppercase*) and weak (*lowercase*) changes in chemical shifts with addition of K4me0/K9me3-containing H3 peptide (NMR) and those that form the K9me3 aromatic cage and K4me0 cage (cage) are shown below. *b*, SPOT-blot peptides corresponding to the amino-terminal tail of histone H3 with or without modification at the Lys-9 position (*1*, monomethylation; *2*, dimethylation; *3*, trimethylation) were probed for binding with different UHRF1 domains. The full-length recombinant UHRF1 and a domain spanning residues 121–286 showed clear binding to the histone tail when Lys-9 was methylated. *c*, FP assays confirm binding of the amino acids 121–286 to a modified peptide corresponding to residues 1–11 of H3 (ARTKQTARKme3ST). *d*, binding of the UHRF1 construct spanning amino acids 121–286 to the series of peptides that have different methylation state of Lys-9 was measured using FP. Peptides corresponding to residues 1–11 of H3, ARTKQTAR[Kme0/1/2/3]ST with Lys-9 unmodified, mono-, di-, or tri-methylated were used. *e*, the TTD is shown in *ribbon* format with TTD$_N$ in *light brown* and TTD$_C$ in *light blue*. A stick representation of the H3K9me3 peptide is shown in *magenta*; electron density was only observed for three residues, R$_8$K$_9$me3S$_{10}$. *f*, close-up view of the aromatic cage in the crystal structures of TTD in its apo form (*green*) and in complex with H3K9me3 (*magenta*). Asp-145 and Asn-194 appear to have some plasticity because their side chains rotate to present the apolar faces toward the ligand, consistent with the ability of the domain to interact with lower states of Lys-9 methylation.

immunostained with Alexa Fluor 555 goat anti-rabbit (Molecular Probes, A21430) and Alexa Fluor 488 goat anti-mouse (Molecular Probes, A11017) secondary antibodies. The cells were again washed in blocking buffer and mounted using Vectashield mounting medium with DAPI (Vector Laboratories, H-1200). The slides were imaged using a Nikon Eclipse E600 microscope, and the images were processed using NIH ImageJ software (35). For the co-localization analysis, background was subtracted using Wright Cell Imaging Facility (WCIF) ImageJ, nuclei with adequate HA staining were identified using the Nucleus Counter plug-in and were then processed with the Intensity Correlation Analysis plug-in (36).

Cell Culture and Western Immunoblotting—Immortalized human vascular smooth muscle cells (HVTs-SM1) were generated as described elsewhere (37) and subcultured in DMEM containing 15% FCS supplemented with 2 mM glutamine, 100 units/ml penicillin and 50 μg/ml streptomycin. Transfections were performed using Lipofectamine (Invitrogen) and 80,000 cells/well in 24-well plates according to the manufacturer's protocols. All experiments described were carried out on cells 24 h after cell transfections with the vector (12 μg/ml).

Mutant full-length human UHRF1 cDNAs, cloned into the pCR-BluntIITOPO, were amplified by PCR using high fidelity Phusion DNA polymerase (Finnzymes, Espoo, Finland) and oligonucleotides flanked with the EcoRI (5′) and XhoI (3′) sites. The PCR products were digested with the corresponding restriction enzymes and further cloned into the pCMV2c vector (Sigma-Aldrich) to obtain FLAG-tagged UHRF1 wild-type and mutants. All of the constructs were verified by sequencing (Proteogenix, Oberhausbergen, France).

Whole-cell extract preparations were described elsewhere (37). Proteins (4 μg) from cell lysates were loaded on one-dimensional SDS-PAGE, 8% for the detection of UHRF1 and 15% for p16[INK4A]. Blots were probed with monoclonal anti-UHRF1 (0.2 μg/ml) or polyclonal anti-p16[INK4A] (1:200) antibodies. The anti-UHRF1 antibody was engineered as described elsewhere (38), whereas anti-p16[INK4A] antibody was obtained from Delta-Biolabs (Gilroy, CA). Secondary HRP-conjugated antibodies were used at 1:5000 dilution. Signals were detected by chemiluminescence using the ECL detection system (Amersham Biosciences).

RESULTS

UHRF1 Contains a Tandem Tudor Domain That Binds H3K9me3 in Vitro—To understand the mechanism by which UHRF1 recognizes H3K9me3, we screened SPOT-blot histone peptide arrays (23) with recombinant UHRF1 and its domains (Fig. 1, *a* and *b*). In agreement with previous studies (8, 13), full-length UHRF1 bound to H3K9me3-containing peptides. However, in contrast to earlier reports (8), the PHD, SRA, or tandem PHD-SRA domains did not interact. Recombinant protein encompassing the region between residues 121 and 286 showed robust binding to methylated H3K9me peptides in SPOT-blot screens, but not to other methyl histone marks, consistent with a recent report (39). FP studies using labeled H3K9me3 peptides (residues 1–12 of H3) confirmed the SPOT-blot results, showing no interaction with either SRA, PHD, or tandem PHD-SRA domains, whereas the conserved, and until

TABLE 1
Crystallographic data collection and refinement statistics

	TTD apo	TTD-H3K9me3
Data collection		
Space group	$P6_2$	$P6_2$
Cell dimensions	a = 98.65, b = 98.65, c = 43.34 Å; α = 90.0, β = 90.0, γ = 120.0°	a = 99.62, b = 99.62, c = 41.23 Å; α = 90.0, β = 90.0, γ = 120.0°
Resolution (Å)	38.7 (2.4)[a]	31.8 (2.4)
R_{sym} or R_{merge}	0.10 (0.45)	0.12 (0.50)
$I/\sigma I$	25.6 (4.7)	22.5 (3.6)
Completeness (%)	99.7 (97.4)	98.8 (92.9)
Redundancy	11.9 (10.9)	6.9 (5.5)
Refinement		
Resolution (Å)	2.4	2.4
No. reflections	9112	8755
R_{work}/R_{free}	0.22/0.28	0.21/0.28
No. of atoms		
Protein	1111	1135
Ligand/ion	1	29
Water	34	73
B-factors		
Protein	85.4	51.6
Ligand/ion	69.8	85.9
Water	71.5	48.9
r.m.s.d.		
Bond lengths (Å)	0.007	0.012
Bond angles	1.055°	1.298°

[a] Highest resolution shell is shown in parentheses.

recently uncharacterized region corresponding to residues 121–286 showed reproducible and robust binding (Fig. 1*c*). Further FP experiments confirmed that this domain favored binding to trimethylated Lys-9 H3 peptide compared with peptides corresponding to lower Lys-9 methylation states (Fig. 1*d*).

We determined the 2.4 Å crystal structure of residues 126–285 of human UHRF1 (PDB code 3DB4, Table 1 and supplemental Fig. S1) revealing a tightly packed pair of Tudor domains (40), each with the signature five-stranded β-barrel fold seen in "Royal" family domains, many of which are involved in the recognition of methylated lysine histone marks (41). The closest structural match is that between the N-terminal subdomain (residues 126–206) and the N-terminal Tudor domain of 53BP1 (PDB code 2G3R; r.m.s.d. of 1.3 Å for 80 Cα positions), including a conserved aromatic cage, which in the case of 53BP1 binds H4K20me2 (42). We therefore hypothesized that recognition of the H3K9me3 mark by UHRF1 could be attributed to the Tandem Tudor Domain (TTD). A second crystal structure of the UHRF1 TTD in complex with a short H3K9me3 peptide (residues 6–11; PDB code 3DB3, Table 1 and Fig. 1*e*), confirmed that the aromatic cage (Phe-152, Tyr-188, and Tyr-191) of the N-terminal Tudor subdomain (TTD$_N$), indeed interacts with the trimethylammonium moiety in the canonical fashion seen in 53BP1 and other Royal family members (41, 42), along with two polar residues, Asn-194 and Asp-145, which complete the binding pocket and provide countercharge. Interestingly, Asp-145 occupies an approximate conserved position that often forms hydrogen bonds with dimethyl ammonium moieties within aromatic cages that recognize lower methylation states such as those of 53PB1 and some malignant brain tumor domains (42–48). However, in UHRF1, the side chain of both Asn-194 and Asp-145 are rotated away from the trimethylammonium moiety of H3K9me3 and participate in an alternative H-bond network to effectively widen the binding pocket and accommodate trimethyllysine (Fig. 1*f*).
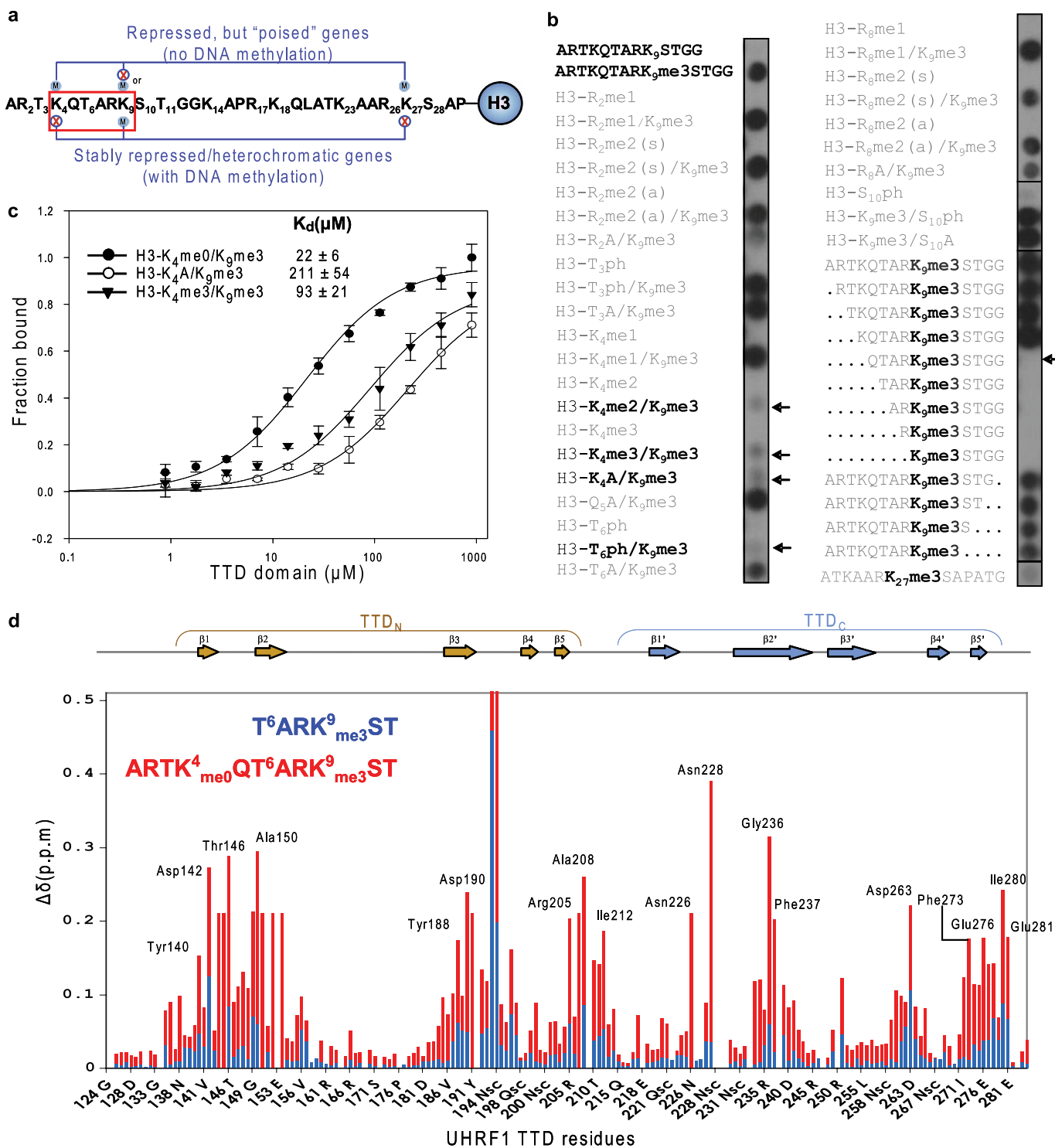
FIGURE 2. **Recognition of multivalent histone signatures associated with heterochromatin by UHRF1.** *a*, schematic representation of the multivalent nature of the histone H3 tail. Residues known to be modified *in vivo* are numbered. Stably repressed genes and heterochromatic regions are characterized by the K4me0/K9me3 state of H3. By contrast, "poised" genes are marked by the bivalent K4me3/K27me3 state accompanied in some cases by K9me3 (72). The region *boxed* in *red* is the key sequence studied here. *b*, a series of H3 peptides were analyzed for binding by the TTD using SPOT-blot arrays. Unmodified H3 peptide (amino acids 1–13) showed no binding, whereas the trimethylated H3K9me3 peptide showed strong binding. The effect of dual modifications, alanine replacement, and deletion (*periods*) in the background of K9me3 was tested. *Arrows* indicate peptides for which binding was lost. *c*, FP assays measuring the binding of the purified TTD to H3 peptides that have Lys-9 trimethylated and Lys-4 that is either mutated or methylated to different degrees. *d*, composite chemical shift changes *versus* residue number for UHRF1 TTD domain after binding to H3 tail K4me0/K9me3-containing long peptide (amino acids 1–11) is indicated in *red*, and shifts observed upon addition of the short peptide (amino acids 6–11) are indicated in *blue*. Prolines and residues that could not be assigned were given a value of zero. Residues that had a very large chemical shift change such that the corresponding peak in the apo form could not be identified were given a constant value of 0.21 ppm. Residues that were strongly affected are listed on the histogram. A large number of residues (37%) is involved in the interaction with the peptide corresponding to the N-terminal tail of the H3 with trimethylated Lys-9 and Lys-4 unmodified.

TTD Recognizes Hallmarks of Heterochromatin—The histone code hypothesis emphasizes the combinatorial nature of histone posttranslational modifications (49). For example, pericentric heterochromatin, which is highly methylated at CpG sites, is characterized not only by high levels of H3K9me3 but also by low levels of modified H3K4 (50–52) (Fig. 2*a*). To explore the possibility that UHRF1 simultaneously recognizes this unique heterochromatic state, an array of doubly-modified and/or mutated H3 peptides was screened for interaction with TTD (Fig. 2*b*). Results showed that in addition to H3K9me3, binding required H3K4 to be either unmodified or monomethylated, whereas di- and trimethylation of Lys-4, its deletion, or substitution with an alanine eliminated binding. Binding was not observed for H3K27me3 peptides encompassing residues 21–33, which contain the ARK$_{27}$S motif (similar to ARK$_9$S) but lack the lysine residue equivalent to the Lys-4 position (Fig. 2*b*). FP assays confirmed these data and showed that binding to H3K4me3/K9me3, although still detectable, showed an ~5-fold lower affinity compared with the H3K4me0/K9me3 peptide (Fig. 2*c*). Likewise, conversion of Lys-4 to alanine reduced the binding affinity by an order of magnitude, highlighting the importance of this residue. Interestingly, Thr-6 phosphorylation also exerted an inhibitory effect on the binding, but Ser-10 phosphorylation did not (Fig. 2*b*).

To confirm the significance of unmodified Lys-4 in the binding specificity of UHRF1, we monitored the NMR spectra of amide resonances of ^{15}N-labeled TTD upon titration with a short H3K9me3 (residues 6–11) and a longer H3K4me0/K9me3 peptide (residues 1–11). The titration data reinforces several key features of the interaction. Consistent with FP studies and the crystal structure, the short H3K9me3 peptide lacking Lys-4 displayed weak binding with dissociation constant, K_d, >1 mM involving only a cluster of residues in and around the aromatic cage (Fig. 2*d* and supplemental Figs. S2 and S3). Titration with the longer H3K4me0/K9me3 peptide, on the other hand, resulted in significantly more chemical shift perturbations with greater values compared with the short peptide, reflecting greater affinity (K_d = 22 μM; Fig. 2*c*). The 2 order of magnitude difference in K_d between short and long peptides indicates an important role for residues upstream of Thr-6 in the peptide, consistent with our SPOT-blot results. Residues affected by addition of the short peptide were a subset of those affected by the addition of the long peptide consistent with the same mode of binding by H3K9me3 in the short and long peptides. The additional residues affected by the long peptide are predominantly those that are at the interface between the TTD$_N$ and TTD$_C$ subdomains and those that link the two subdomains. The extensive nature of the chemical shift changes, including buried residues at the interface between TTD$_N$ and TTD$_C$ that are not surface exposed, suggests a conformational adjustment of the two subdomains relative to one another to accommodate a multivalent histone tail.

Structural Basis for Recognition of H3K4me0/K9me3 Signature—To determine the mechanism by which H3K4 contributes to the interaction between TTD and H3, we attempted to crystallize UHRF1 TTD with H3K4me0/H3K9me3 peptides. Despite repeated attempts, we were unable to obtain crystals in the presence of the longer peptides. As an alternative method,

TABLE 2
NMR data and refinement statistics

	TTD-H3K4me0/K9me3
NMR distance and dihedral constraints	
Distance restraints	
Total NOE	3352
Intra-residue	658
Inter-residue	2664
Sequential ($i–j = 1$)	969
Nonsequential ($i–j > 1$)	1695
Hydrogen bonds	71
Protein-peptide intermolecular	30
Total dihedral angle restraints	256
Protein	
ϕ	130
ψ	126
Total RDCs	416
Structure statistics	
Violations (mean and S.D.)	
Distance constraints (Å)	0.0435 ± 0.0117
Dihedral angle constraints	3.3492 ± 0.4605°
Max. dihedral angle violation	4.4468°
Max. distance constraint violation (Å)	0.0747
Deviations from idealized geometry	
Bond lengths (Å)	0.0144 ± 0.0002
Bond angles	1.2976 ± 0.0253°
Impropers	3.24 ± 0.13°
Average pairwise r.m.s.d.[a] (Å)	
Protein	
Heavy	1.40 ± 0.13
Backbone	0.76 ± 0.18
Peptide	
Heavy	1.99 ± 0.35
Backbone	0.77 ± 0.19
Complex	
Heavy	1.47 ± 0.13
Backbone	0.81 ± 0.16

[a] Ensemble of 15 lowest energy structures out of 100 used in r.m.s.d. calculations. For the UHRF1 TTD protein, residues 135–160 and 183–281 were used; for the H3K4me0K9me3 peptide, residues 4–10 were used.

we used NMR spectroscopy to obtain the solution structure of the UHRF1 TTD (residues 124–285) in complex with a H3K4me0/H3K9me3 peptide (residues 1–11) (PDB code 2L3R; Table 2 and Figs. 3 and 4). Both Tudor subdomains formed extensive interactions with the peptide involving side chains of K9me3, Thr-6 and Lys-4 (Fig. 3), which resembles the cooperation between the two chromodomains of CHD1 that form a single pocket to recognize an extended methylated histone tail (53).

The K9me3 side chain sits within the conserved aromatic cage of TTD$_N$ as seen in our crystal structure with the short peptide (supplemental Fig. S5*b*). H3 residues amino-terminal to K9me3 extend along a shallow groove at the interface between the two Tudor subdomains (Fig. 3*a*). The side chain of Lys-4 is recognized by a network of hydrogen bonds from carboxylates of Asp-142 and Glu-153 (Fig. 3, *c* and *d*). This recognition mode of the unmodified H3 Lys-4 is similar to that of PHD domains (5, 54, 55). Although monomethylation can be tolerated, di- or trimethylation would be expected to disrupt this hydrogen bond network and also sterically interfere with binding, consistent with our SPOT-blot and FP results. However, unlike many H3K4 recognition motifs, the TTD does not interact with the N-terminal NH3$^+$ moiety. Interestingly, phosphorylation of Thr-6, which has been shown to prevent the demethylation of H3K4 (56), would be expected to introduce both steric clashes and electrostatic repulsion (Fig. 3*b*). The extensive interactions with Lys-4 and Thr-6 upstream of the ARKS motif common to Lys-9 and Lys-27 explain the selectivity of UHRF1
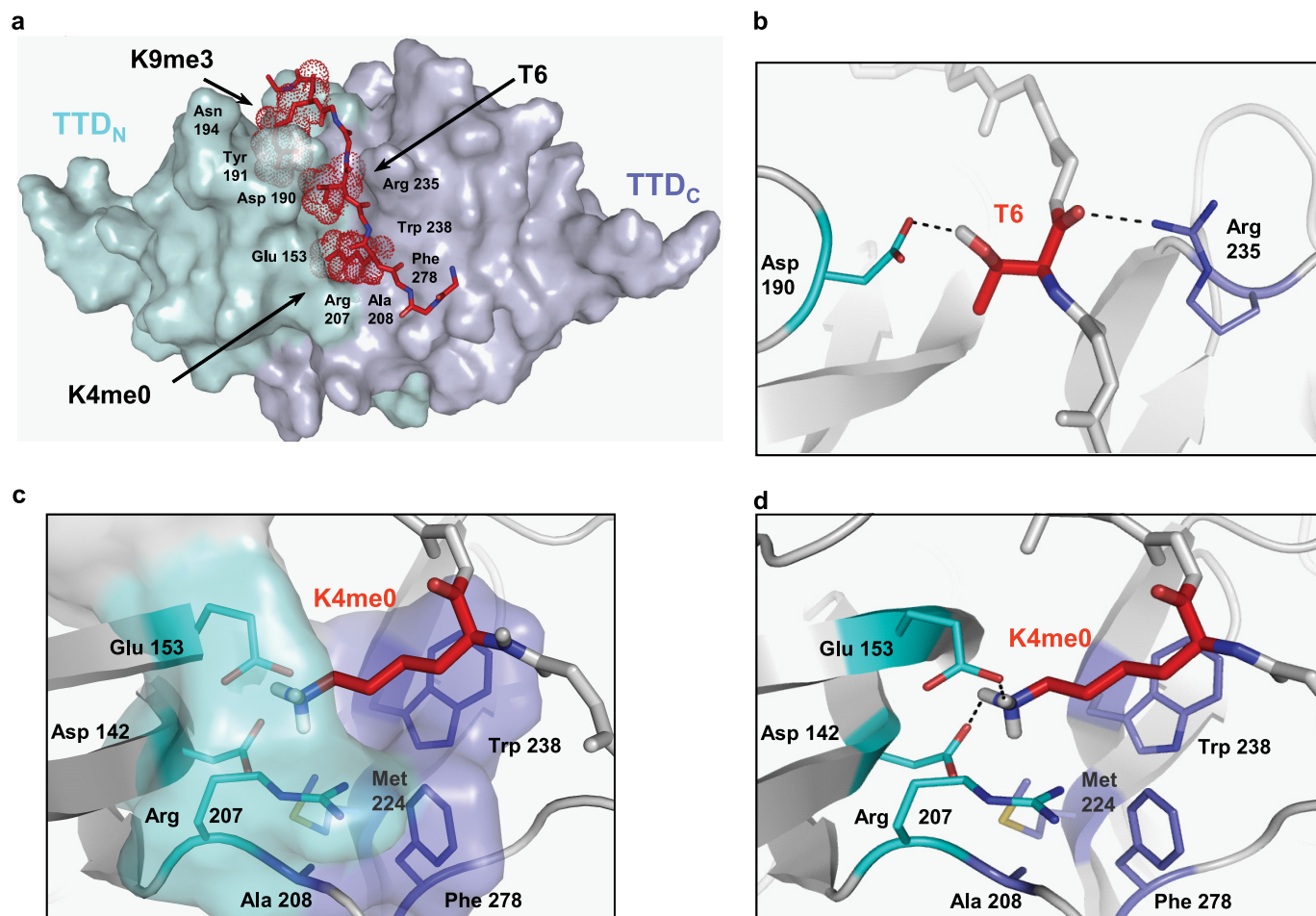
FIGURE 3. **Recognition of multivalent sites at the interface between the two Tudor subdomains.** *a*, surface representation of the lowest energy complex NMR structure of TTD bound to the histone H3 tail. The N- and C-terminal Tudor subdomains of UHRF1 are shown in *cyan* and *slate* colors, respectively. Key residues on the peptide are shown as *red dots*. *b*, the TTD-H3 binding is stabilized by the interaction between the hydroxyl and backbone carbonyl groups of H3 Thr-6 that hydrogen bond with UHRF1 Asp-190 carboxylate and the Arg-235 guanidinium groups, respectively. Only protons participating in hydrogen bonding are shown. *c*, the H3K4me0 pocket is formed by a hydrophilic wall (residues from TTD$_N$, Asp-142 and Glu-153), an aromatic wall (TTD$_C$, Trp-238 and Phe-278), as well as Met-224 and residues from the linker between the two subdomains Arg-207 and Ala-208. *d*, detailed interactions between the TTD and K4me0 showing the side chain of Lys-4 is "caged" by two hydrogen bonds.

TTD for K9me3 over K27me3. Heteronuclear NOE values showed that in solution, the linker between TTD$_N$ and TTD$_C$ does not undergo motions faster than the TTD as a whole and therefore does not behave as a flexible linker (supplemental Fig. S4). Thus, the TTD behaves as a single domain to recognize a single histone tail with the H3K4me0/K9me3 modification state as opposed to recognition of two separate H3 tails with the K4me0 and K9me3 states. This suggests that there may be cellular mechanisms for coordination of the modifications at the Lys-4 and Lys-9 sites on individual histone H3 tails.

Reorientation of TTD Subdomains upon Histone H3 Binding—Overlay of the backbone atoms of TTD$_N$ in the apo crystal structure and the lowest energy member of the solution ensemble of the TTD-H3K4me0/K9me3 complex revealed a rigid body movement of the second subdomain relative to the first (Fig. 4, *b* and *c*). Although TTD$_N$ in the apo and bound conformations had only minor differences with an r.m.s.d. of 0.77 Å, superposition of the entire TTD revealed a 2-fold greater discrepancy between the structures with r.m.s.d. of 1.37 Å (Fig. 4*e*). In the bound form, we observed an adjustment of the TTD$_C$ corresponding to a 4.2 Å movement of the tip of the α1′ helix,

and smaller shifts in the β1′–β2′ and the β2′–β3′ loops (Fig. 4*c*). This difference in subdomain orientations was also observed between the solution structure and the x-ray structure bound to the short H3K9me3 peptide, suggesting that the two TTD subdomains adjust their relative orientation for optimal recognition of the longer bivalent H3K4me0/K9me3 peptide (supplemental Fig. S5*a*).

Residual dipolar couplings (RDC) measurements give direct information about the orientation of bond vectors relative to the molecular alignment tensor and are extremely sensitive to the relative orientations of domains within a protein (57, 58). Our solution structure of the H3K4me0/K9me3-bound TTD was refined using five sets of RDCs (three sets of ^{15}N-^{1}HN, and ^{13}C′-^{13}CA, ^{15}N-^{13}C′ data sets) to more accurately determine the relative orientations of the two subdomains. Analysis of these RDC measurements with respect to the apo crystal structure showed that they had a significantly poorer fit with the apo structure, indicating that the bond vectors in the TTD-H3K4me0/K9me3 solution ensemble do not correspond well with the apo crystal structure (Fig. 4*d* and supplemental Fig. S6). The apoprotein in solution suffers from selective line
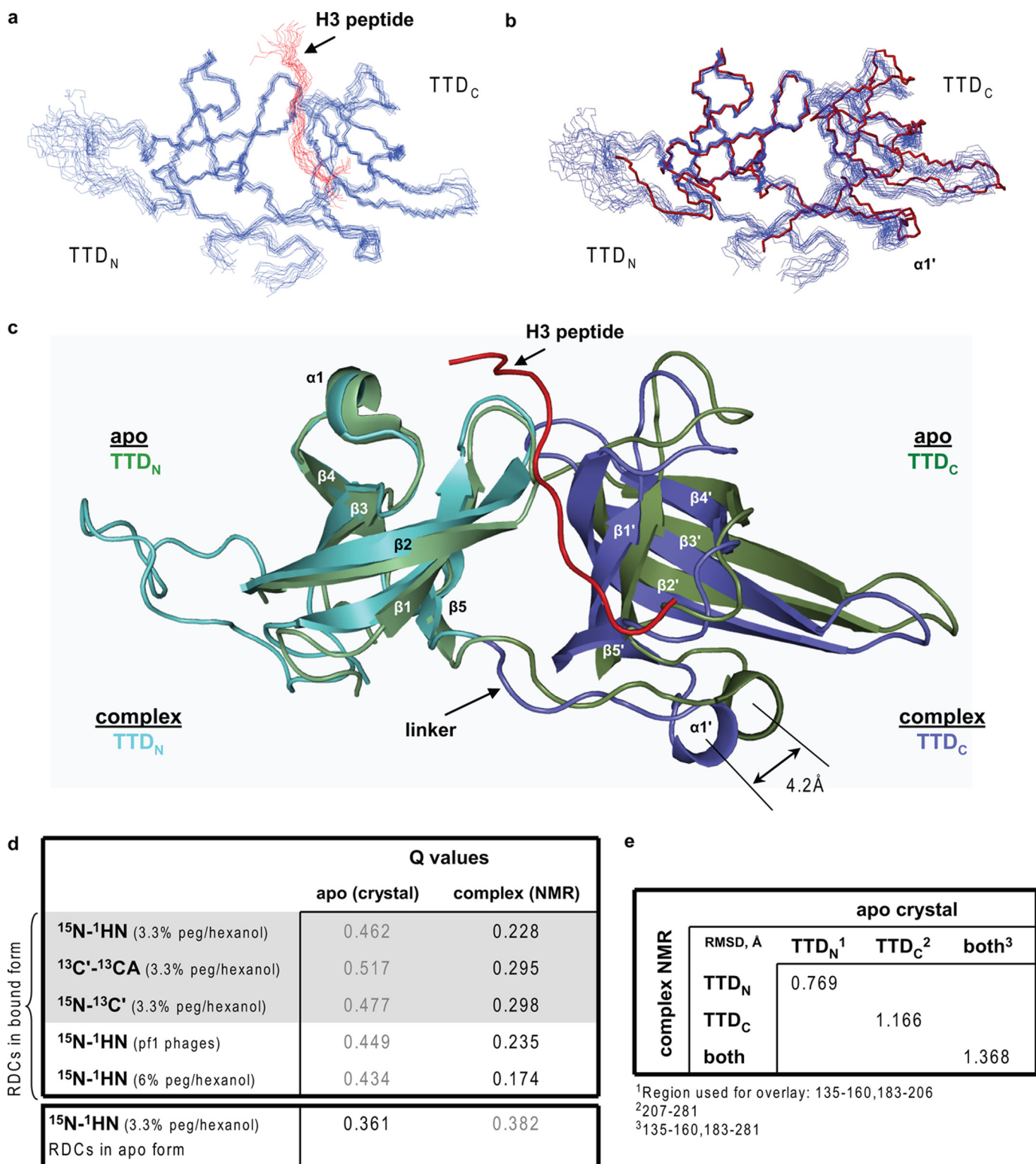
FIGURE 4. **Structural readjustment of TTD_C to accommodate the histone tail.** *a*, solution NMR ensemble (15 structures) of the complex structure showing the polypeptide backbone of TTD (*blue*) and histone peptide (*red*). The structures were overlaid over the region within TTD residues 139–161 and 182–279. *b*, overlay of the solution TTD ensemble (residues 139–161 and 182–206) in the bound form (*blue*) and x-ray apo structure (*red*). *c*, overlay of the apo crystal structure (*green*) and complex NMR structure (*blue*). The N and C termini are removed for clarity to better show the linker between the TTD subdomains. The extent of the TTD_C shift relative to TTD_N upon recognition of the H3K4me0/K9me3 peptide is indicated. *d*, goodness of the fit between the experimental RDC values measured for either the H3K4me0/K9me3-bound TTD or apo-TTD in solution and the predicted values for the NMR solution structure and apo crystal structures. For couplings highlighted in *gray*, the same alignment tensor was used for fitting. *e*, the r.m.s.d. (Å) between the apo crystal structure and lowest energy structure of the ensemble of TTD complex solution structures was calculated with MolMol.
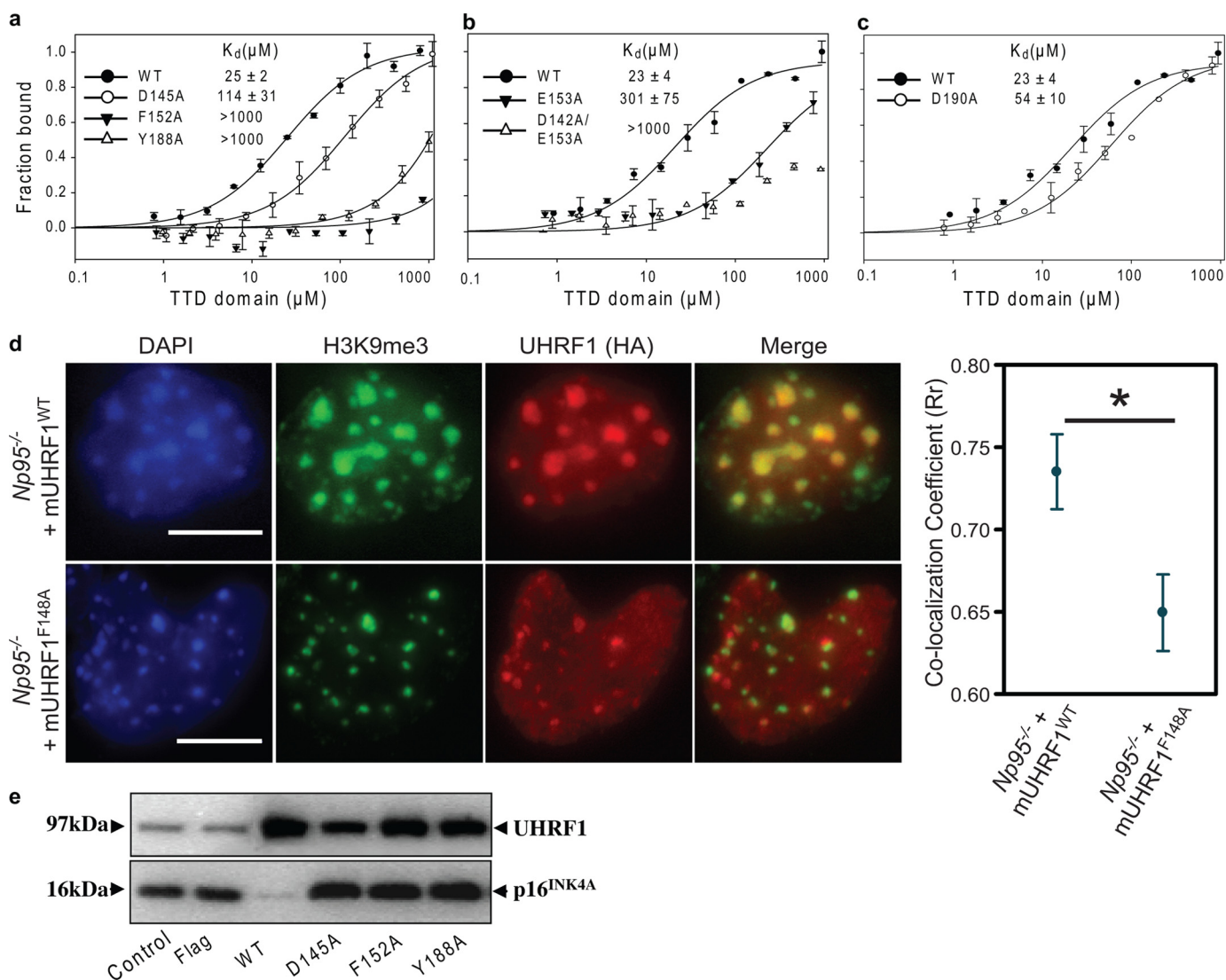
FIGURE 5. **Mutational analysis confirms localization of TTD to heterochromatin in mouse ES cells.** *a–c*, binding of wild-type and mutant TTD forms that disrupt the H3K9me3 binding cage (*a*), H3K4me0 binding cage (*b*), or Thr-6 recognition within the recombinant human TTD (*c*). The fluorescence polarization binding assays were performed using a long, H3K4me0/K9me3-containing histone peptide (amino acids 1–11). *d*, stably integrated mouse $Np95^{-/-}$ ES cell lines expressing HA-tagged wild-type mUHRF1 (*top panel*) or mUHRF1^{F148A} (*lower panel*) were stained for HA, H3K9me3, and DAPI. The F148A mutation in mouse protein is equivalent to F152A in human protein. The extent of mUHRF1 co-localization with H3K9me3 was quantitatively evaluated using 60 independent nuclei selected in an unbiased manner by the ImageJ Nucleus Counter plug-in. The HA-mUHRF1^{F148A} protein shows a significantly reduced correlation coefficient compared with the wild-type protein (*p* value = 0.0102, average and S.D. are shown). *e*, effect of UHRF1 wild-type and mutant TTD proteins on p16^{INK4A} protein levels in immortalized human vascular smooth muscle cells (HVTs-SM1). Membranes were probed with an anti-UHRF1 monoclonal antibody, accounting for the presence of an endogenous UHRF1 band in the negative control and vector only transfected cells (FLAG). The blot shown here is representative of at least three independent experiments.

broadening, especially at the interface between TTD_N and TTD_C and was less amenable to a detailed RDC analysis. Nevertheless, a single RDC data set collected on the apoprotein in solution has a better fit to the apo crystal structure (compared with the RDCs collected on the TTD bound to H3K4me0/K9me3). Similarly, small angle x-ray scattering of the apo and H3K4me0-K9me3 solution complex also showed differences between the apo and H3K4me0/K9me3-bound structures (supplemental Fig. S7). Taken together, the solution and x-ray data support a conformational adjustment of the two TTD subdomains relative to one another upon peptide binding, further underscoring the importance of the intersubdomain peptide binding groove.

Mutational Analysis Confirms Localization of TTD to Heterochromatin in Vivo—To investigate the biological relevance of UHRF1 TTD, we generated mutant protein and tested the

binding to histone H3 peptides. Mutations within the canonical aromatic cage disrupted the binding greatly, and K_d values could not be accurately determined (Fig. 5*a*). Mutations of Asp-142 and Glu-153, residues that contribute to the hydrogen bond network with H3K4me0, disrupt the interaction with the H3 tail without affecting the protein folding (Fig. 5*b* and supplemental Fig. S8*a*). Lastly, mutation of TTD residue interacting with H3T6 leads to the diminished interaction observed by FP assays (Fig. 5*c* and supplemental Fig. S8*b*).

UHRF1 localizes to and contributes to the shape and density of pericentric heterochromatin (6–12), which is typically condensed in DAPI-bright chromocenters that are enriched with the H3K9me3 modification (59). To determine whether the TTD contributes to the localization of UHRF1 to H3K9me3-enriched regions in cells, we stably expressed cDNAs for the

wild-type murine UHRF1 (mUHRF1WT; Np95) and a mutant defective for H3K9me3 binding, mUHRF1^{F148A} (mF148 is equivalent to hF152) in $Np95^{-/-}$ ES cells (6, 7, 60). The wild-type protein was localized almost exclusively to the DAPI-bright, H3K9me3-rich chromocenters, as expected (Fig. 5*d*). However, the mUHRF1^{F148A} mutant protein consistently showed a slightly more diffuse localization throughout the nucleus even though staining at the pericentric heterochromatin could often be observed. The extent of co-localization between the wild-type and mutated mUHRF1 proteins and H3K9me3 foci was further quantified and revealed that the mUHRF1^{F148A} mutant protein indeed showed a significantly reduced co-localization with H3K9me3 foci (p value = 0.0102) (Fig. 5*d*). This indicates that the TTD domain can assist the localization of UHRF1 to H3K9me3-marked heterochromatin regions in a manner dependent on the integrity of its trimethyllysine-binding aromatic cage.

UHRF1 also participates in macromolecular complexes containing repressive histone factors such as methyltransferases G9a, GLP, SUV39H1, and HDAC1 and contributes to transcriptional gene silencing, as demonstrated, for instance, for the *p16*^{INK4A} tumor suppressor gene (15, 37, 61). We therefore investigated whether H3K9me3 binding by the TTD contributes to down-regulation of p16^{INK4A} protein levels by transfecting immortalized human vascular smooth muscle cells with wild-type or TTD-mutated UHRF1 variants and analyzing protein levels by Western blots. As expected, overexpression of wild-type FLAG-tagged UHRF1 protein reproducibly resulted in reduction of p16^{INK4A} levels (Fig. 5*e*). On the other hand, TTD aromatic cage mutants deficient for H3K9me3 binding failed to reduce the levels of *p16*^{INK4A}. These data suggest that H3K9me3 binding by the TTD domain contributes to the regulation of target gene expression by UHRF1.

DISCUSSION

The Tudor domain is found in many proteins involved in epigenetic regulation and can exist in isolation, in tandem, or even as a triad (62, 63). Comparison with other proteins that contain tandem Tudor domains suggests that although they all have the canonical five-strand β-barrel fold, additional secondary structure elements and the relative orientation and topology of the two domains provide unique features and great versatility among this family (supplemental Fig. S10). To our knowledge, interdomain movement accompanying histone peptide recognition by effector domains has not been described previously. For example, recognition of histone tails by the double chromodomains of CHD1 (53), tandem Tudor domains of FXR2 (64), 53BP1 (42), JMJD2A (65), or Sgf29 (PDB: 3MEU), and tandem PHD fingers of DPF3b (66) do not require the adjustment of the two domains. The recognition of two acetylation marks by a single Brdt (67) seems to preserve the overall fold, and the combinatorial rheostat-like readout of H3K4me3/T6ph by ING2 PHD finger (68) does not appear to involve structural rearrangement within the PHD finger. Thus, previous modes of effector domain-histone peptide binding show minimal structural perturbations and can be described as either "surface recognition" or "cavity insertion" models, but neither involves subdomain rearrangements as observed here (63, 69).

Taken together, these data support a model in which the simultaneous readout of the H3K4 and H3K9 modification states by the TTD is achieved by a single domain that undergoes a conformational change to accommodate both lysines. There is increasing evidence for coordination of the posttranslational status of H3K4 and H3K9 in mammalian cells. Binda *et al.* (51) recently reported that the H3K9 methyltransferases, SETDB1, SUV39H1, G9a, and GLP preferentially methylate Lys-9 of H3 histones that are depleted in the K4me2/3 mark. This indicates cross talk between H3K4 and H3K9 in the writing of the H3K9me3 mark, and it therefore stands to reason that "reader" domains may have also evolved to read the status of both Lys-4 and Lys-9. It was recently reported that the ATRX-DNMT3-DNMT3L (ADD) domain of ATRX can recognize the H3K4me0/K9me3 signature and may play a role in localizing ATRX to DAPI-dense chromo centers similar to that seen here for UHRF1 (70). Furthermore, Bartke *et al.* (3) recently showed that although UHRF1 from cellular extracts was enriched for binding recombinant nucleosomes containing methyl-CpG (presumably via its SRA domain), UHRF1 was also highly enriched at nucleosomes without CpG methylation, but only if they contained the H3K4me0/K9me3 modification signature. There was no enrichment of UHRF1 at H3K4me3 nucleosomes even if the DNA contained methyl-CpG (3). These observations are consistent with an important role for the TTD in contributing to the subnuclear localization of UHRF1 in addition to the SRA domain (39). Given the critical role played by UHRF1 in maintenance DNA methylation, our work suggests that the H3K4me0/K9me3 signature is highly associated with methylated DNA, which is consistent with observations for heterochromatic regions and stably repressed genes. By contrast, other chromatin states associated with transcriptional repression such as bivalent domains (71, 72) or Polycomb-repressed domains (32) are not expected to undergo similar coupling between DNA and histone modifications, thus ensuring more dynamic expression trajectories through development.

REFERENCES

1. Denslow, S. A., and Wade, P. A. (2007) *Oncogene* **26,** 5433–5438
2. Klose, R. J., and Bird, A. P. (2006) *Trends Biochem. Sci.* **31,** 89–97
3. Bartke, T., Vermeulen, M., Xhemalce, B., Robson, S. C., Mann, M., and Kouzarides, T. (2010) *Cell* **143,** 470–484
4. Meissner, A., Mikkelsen, T. S., Gu, H., Wernig, M., Hanna, J., Sivachenko, A., Zhang, X., Bernstein, B. E., Nusbaum, C., Jaffe, D. B., Gnirke, A., Jaenisch, R., and Lander, E. S. (2008) *Nature* **454,** 766–770
5. Ooi, S. K., Qiu, C., Bernstein, E., Li, K., Jia, D., Yang, Z., Erdjument-Bromage, H., Tempst, P., Lin, S. P., Allis, C. D., Cheng, X., and Bestor, T. H. (2007) *Nature* **448,** 714–717
6. Bostick, M., Kim, J. K., Estève, P. O., Clark, A., Pradhan, S., and Jacobsen, S. E. (2007) *Science* **317,** 1760–1764
7. Sharif, J., Muto, M., Takebayashi, S., Suetake, I., Iwamatsu, A., Endo, T. A., Shinga, J., Mizutani-Koseki, Y., Toyoda, T., Okamura, K., Tajima, S., Mitsuya, K., Okano, M., and Koseki, H. (2007) *Nature* **450,** 908–912

8. Karagianni, P., Amazit, L., Qin, J., and Wong, J. (2008) *Mol. Cell. Biol.* **28,** 705–717

9. Miura, M., Watanabe, H., Sasaki, T., Tatsumi, K., and Muto, M. (2001) *Exp. Cell Res.* **263,** 202–208

10. Papait, R., Pistore, C., Grazini, U., Babbio, F., Cogliati, S., Pecoraro, D., Brino, L., Morand, A. L., Dechampesme, A. M., Spada, F., Leonhardt, H., McBlane, F., Oudet, P., and Bonapace, I. M. (2008) *Mol. Biol. Cell* **19,** 3554–3563

11. Papait, R., Pistore, C., Negri, D., Pecoraro, D., Cantarini, L., and Bonapace, I. M. (2007) *Mol. Biol. Cell* **18,** 1098–1106

12. Uemura, T., Kubo, E., Kanari, Y., Ikemura, T., Tatsumi, K., and Muto, M. (2000) *Cell Struct. Funct.* **25,** 149–159

13. Citterio, E., Papait, R., Nicassio, F., Vecchi, M., Gomiero, P., Mantovani, R., Di Fiore, P. P., and Bonapace, I. M. (2004) *Mol. Cell. Biol.* **24,** 2526–2535

14. Kim, J. K., Estève, P. O., Jacobsen, S. E., and Pradhan, S. (2009) *Nucleic Acids. Res.* **37,** 493–505

15. Unoki, M., Nishidate, T., and Nakamura, Y. (2004) *Oncogene.* **23,** 7601–7610

16. Woo, H. R., Pontes, O., Pikaard, C. S., and Richards, E. J. (2007) *Genes Dev.* **21,** 267–277

17. Otwinowski, Z., and Minor, W. (1997) *Macromolecular Crystallography, Pt A* **276,** 307–326

18. Terwilliger, T. C., and Berendzen, J. (1999) *Acta Crystallogr. D Biol. Crystallogr.* **55,** 849–861

19. Terwilliger, T. C. (2003) *Acta Crystallogr. D Biol. Crystallogr.* **59,** 38–44

20. Emsley, P., and Cowtan, K. (2004) *Acta Crystallogr. D Biol. Crystallogr.* **60,** 2126–2132

21. Murshudov, G. N., Vagin, A. A., and Dodson, E. J. (1997) *Acta Crystallogr. D Biol. Crystallogr.* **53,** 240–255

22. Painter, J., and Merritt, E. A. (2006) *J. Appl. Crystallogr.* **39,** 109–111

23. Nady, N., Min, J., Kareta, M. S., Chédin, F., and Arrowsmith, C. H. (2008) *Trends Biochem. Sci* **33,** 305–313

24. Gutmanas, A., Jarvoll, P., Orekhov, V. Y., and Billeter, M. (2002) *J. Biomol. NMR.* **24,** 191–201

25. Orekhov, V. Y., Ibraghimov, I., and Billeter, M. (2003) *J. Biomol. NMR.* **27,** 165–173

26. Delaglio, F., Grzesiek, S., Vuister, G. W., Zhu, G., Pfeifer, J., and Bax, A. (1995) *J. Biomol. NMR.* **6,** 277–293

27. Goddard, T. D., and Kneller, D. G. (2006) SPARKY 3, v.3.113, University of California, San Francisco

28. Ottiger, M., Delaglio, F., and Bax, A. (1998) *J. Magn. Reson.* **131,** 373–378

29. Mittermaier, A., and Kay, L. E. (2001) *J. Am. Chem. Soc.* **123,** 6892–6903

30. Rückert, M., and Otting, G. (2000) *JACS* **122,** 7793–7797

31. Hansen, M. R., Mueller, L., and Pardi, A. (1998) *Nat. Struct. Biol.* **5,** 1065–1074

32. Schuettengruber, B., Chourrout, D., Vervoort, M., Leblanc, B., and Cavalli, G. (2007) *Cell* **128,** 735–745

33. Zweckstetter, M. (2008) *Nat. Protoc.* **3,** 679–690

34. Dosset, P., Hus, J. C., Marion, D., and Blackledge, M. (2001) *J. Biomol. NMR* **20,** 223–231

35. Abramoff, M. D., Magalhaes, P. J., Ram, S. J. (2004) *Biophotonics International* **11,** 36–42

36. Li, Q., Lau, A., Morris, T. J., Guo, L., Fordyce, C. B., and Stanley, E. F. (2004) *J. Neurosci.* **24,** 4070–4081

37. Achour, M., Jacq, X., Rondé, P., Alhosin, M., Charlot, C., Chataigneau, T., Jeanblanc, M., Macaluso, M., Giordano, A., Hughes, A. D., Schini-Kerth, V. B., and Bronner, C. (2008) *Oncogene* **27,** 2187–2197

38. Hopfner, R., Mousli, M., Jeltsch, J. M., Voulgaris, A., Lutz, Y., Marin, C., Bellocq, J. P., Oudet, P., and Bronner, C. (2000) *Cancer. Res.* **60,** 121–128

39. Rottach, A., Frauer, C., Pichler, G., Bonapace, I. M., Spada, F., and Leonhardt, H. (2010) *Nucleic. Acids. Res.* **38,** 1796–1804

40. Hashimoto, H., Horton, J. R., Zhang, X., and Cheng, X. (2009) *Epigenetics.* **4,** 8–14

41. Maurer-Stroh, S., Dickens, N. J., Hughes-Davies, L., Kouzarides, T., Eisenhaber, F., and Ponting, C. P. (2003) *Trends Biochem. Sci.* **28,** 69–74

42. Botuyan, M. V., Lee, J., Ward, I. M., Kim, J. E., Thompson, J. R., Chen, J., and Mer, G. (2006) *Cell* **127,** 1361–1373

43. Grimm, C., de Ayala Alonso, A. G., Rybin, V., Steuerwald, U., Ly-Hartig, N., Fischle, W., Müller, J., and Müller, C. W. (2007) *EMBO Rep.* **8,** 1031–1037

44. Grimm, C., Matos, R., Ly-Hartig, N., Steuerwald, U., Lindner, D., Rybin, V., Müller, J., and Müller, C. W. (2009) *EMBO J.* **28,** 1965–1977

45. Guo, Y., Nady, N., Qi, C., Allali-Hassani, A., Zhu, H., Pan, P., Adams-Cioaba, M. A., Amaya, M. F., Dong, A., Vedadi, M., Schapira, M., Read, R. J., Arrowsmith, C. H., and Min, J. (2009) *Nucleic Acids Res.* **37,** 2204–2210

46. Li, H., Fischle, W., Wang, W., Duncan, E. M., Liang, L., Murakami-Ishibe, S., Allis, C. D., and Patel, D. J. (2007) *Mol. Cell.* **28,** 677–691

47. Min, J., Allali-Hassani, A., Nady, N., Qi, C., Ouyang, H., Liu, Y., MacKenzie, F., Vedadi, M., and Arrowsmith, C. H. (2007) *Nat. Struct. Mol. Biol.* **14,** 1229–1230

48. Santiveri, C. M., Lechtenberg, B. C., Allen, M. D., Sathyamurthy, A., Jaulent, A. M., Freund, S. M., and Bycroft, M. (2008) *J. Mol. Biol.* **382,** 1107–1112

49. Strahl, B. D., and Allis, C. D. (2000) *Nature* **403,** 41–45

50. Agalioti, T., Chen, G., and Thanos, D. (2002) *Cell* **111,** 381–392

51. Binda, O., LeRoy, G., Bua, D. J., Garcia, B. A., Gozani, O., and Richard, S. (2010) *Epigenetics.* **5,** 767–775

52. Chen, W. Y., and Townes, T. M. (2000) *Proc. Natl. Acad. Sci. U.S.A.* **97,** 377–382

53. Flanagan, J. F., Mi, L. Z., Chruszcz, M., Cymborowski, M., Clines, K. L., Kim, Y., Minor, W., Rastinejad, F., and Khorasanizadeh, S. (2005) *Nature* **438,** 1181–1185

54. Lan, F., Collins, R. E., De Cegli, R., Alpatov, R., Horton, J. R., Shi, X., Gozani, O., Cheng, X., and Shi, Y. (2007) *Nature* **448,** 718–722

55. Otani, J., Nankumo, T., Arita, K., Inamoto, S., Ariyoshi, M., and Shirakawa, M. (2009) *EMBO Rep.* **10,** 1235–1241

56. Metzger, E., Imhof, A., Patel, D., Kahl, P., Hoffmeyer, K., Friedrichs, N., Müller, J. M., Greschik, H., Kirfel, J., Ji, S., Kunowska, N., Beisenherz-Huss, C., Günther, T., Buettner, R., and Schüle, R. (2010) *Nature* **464,** 792–796

57. Bax, A., Kontaxis, G., and Tjandra, N. (2001) *Methods. Enzymol.* **339,** 127–174

58. Prestegard, J. H., Bougault, C. M., and Kishore, A. I. (2004) *Chem. Rev* **104,** 3519–3540

59. Krauss, V. (2008) *Genetica.* **133,** 93–106

60. Muto, M., Kanari, Y., Kubo, E., Takabe, T., Kurihara, T., Fujimori, A., and Tatsumi, K. (2002) *J. Biol. Chem.* **277,** 34549–34555

61. Suzuki, M., Sunaga, N., Shames, D. S., Toyooka, S., Gazdar, A. F., and Minna, J. D. (2004) *Cancer Res.* **64,** 3137–3143

62. Adams-Cioaba, M. A., and Min, J. (2009) *Biochem. Cell Biol.* **87,** 93–105

63. Taverna, S. D., Li, H., Ruthenburg, A. J., Allis, C. D., and Patel, D. J. (2007) *Nat. Struct. Mol. Biol.* **14,** 1025–1040

64. Adams-Cioaba, M. A., Guo, Y., Bian, C., Amaya, M. F., Lam, R., Wasney, G. A., Vedadi, M., Xu, C., and Min, J. (2010) *PLoS One* **5,** e13559

65. Huang, Y., Fang, J., Bedford, M. T., Zhang, Y., and Xu, R. M. (2006) *Science* **312,** 748–751

66. Zeng, L., Zhang, Q., Li, S., Plotnikov, A. N., Walsh, M. J., and Zhou, M. M. (2010) *Nature* **466,** 258–262

67. Morinière, J., Rousseaux, S., Steuerwald, U., Soler-López, M., Curtet, S., Vitte, A. L., Govin, J., Gaucher, J., Sadoul, K., Hart, D. J., Krijgsveld, J., Khochbin, S., Müller, C. W., and Petosa, C. (2009) *Nature* **461,** 664–668

68. Garske, A. L., Oliver, S. S., Wagner, E. K., Musselman, C. A., LeRoy, G., Garcia, B. A., Kutateladze, T. G., and Denu, J. M. (2010) *Nat. Chem. Biol.* **6,** 283–290

69. Ruthenburg, A. J., Li, H., Patel, D. J., and Allis, C. D. (2007) *Nat. Rev. Mol. Cell Biol.* **8,** 983–994

70. Dhayalan, A., Tamas, R., Bock, I., Tattermusch, A., Dimitrova, E., Kudithipudi, S., Ragozin, S., and Jeltsch, A. (2011) *Hum. Mol. Genet.*, in press

71. Bernstein, B. E., Mikkelsen, T. S., Xie, X., Kamal, M., Huebert, D. J., Cuff, J., Fry, B., Meissner, A., Wernig, M., Plath, K., Jaenisch, R., Wagschal, A., Feil, R., Schreiber, S. L., and Lander, E. S. (2006) *Cell* **125,** 315–326

72. Bilodeau, S., Kagey, M. H., Frampton, G. M., Rahl, P. B., and Young, R. A. (2009) *Genes. Dev.* **23,** 2484–2489